



Supporting Online Material for

Nanoscale Tunable Reduction of Graphene Oxide for Graphene Electronics

Zhongqing Wei, Debin Wang, Suenne Kim, Soo-Young Kim, Yike Hu, Michael K. Yakes, Arnaldo R. Laracuente, Zhenting Dai, Seth R. Marder, Claire Berger, William P. King, Walter A. de Heer, Paul E. Sheehan,* Elisa Riedo*

*To whom correspondence should be addressed. E-mail: paul.sheehan@nrl.navy.mil;
elisa.riedo@physics.gatech.edu

Published 11 June 2010, *Science* **328**, 1373 (2010)
DOI: 10.1126/science.1188119

This PDF file includes:

Materials and Methods
Figs. S1 to S8
References and Notes

1. GO flakes and GO_{epi}

A dispersion of GO flakes was prepared via the modified Hummer method (1). The dispersion in deionized water was then drop-cast onto SiO_x/Si substrate and blown dry with N₂.

Epitaxial graphene layers were grown on the C-face of 4H-SiC (insulating wafers from CREE) by thermal decomposition at high temperature in an RF induction furnace (2). The samples consist typically of 5-20 layers stacked with non graphitic orientational order (3). The epitaxial graphene films were oxidized directly on chip by the Hummer's method (4), as described in Ref. (1). After oxidation the previously conducting and light grey color EG films (square resistance $R \sim 100\text{-}200 \text{ M}\Omega$) become non-conducting ($R \gg 500 \text{ M}\Omega$) and yellowish transparent. AFM pictures reveal that the morphology of the films is essentially preserved. A complete electrical characterization of GO_{epi} was reported in the supplementary information of Ref. (1) where a Schottky barrier of about 0.5 eV was found.

The electrical resistivity values of SiC substrates of the samples used in the paper are $10^5 \text{ }\Omega \text{ cm}^{-1}$ (Fig. 3 and Fig. 4C), $10^8 \text{ }\Omega \text{ cm}^{-1}$ (Fig. 4A and 4B) and $10^9 \text{ }\Omega \text{ cm}^{-1}$ (Fig. S7). The

average numbers of epitaxially grown graphene layers of the samples used in the paper are determined by ellipsometry and/or AFM topography imaging as: 30 (Fig. 3), 16 (Fig. 4A and 4B), 13 (Fig. 4C,), and 3 (Fig. S7).

2. TCNL and AFM characterizations

Custom made thermal AFM cantilevers (5) were used to carry out TCNL. The nominal spring constant of these thermal cantilevers is 0.5 N m^{-1} . In Fig. 1 and Fig. 2, TCNL was performed in N_2 environment using a Veeco Multimode III AFM. In Fig. 3 and Fig. 4, TCNL was performed in ambient conditions using a Veeco Multimode IV AFM. During the TCNL process, the thermal cantilever was heated while the tip is in contact with the GO surface. The loading force applied to the cantilever is in the range of 120–230 nN.

Veeco AFMs (Multimode III and IV) were used for performing friction FFM, CAFM, and KPFM. Friction measurements were performed using a silicon nitride probe (spring constant: 0.1 N m^{-1} ; MSCT-AUHW, Veeco), in a N_2 environment at room temperature, at a scanning speed of $9.5 \text{ } \mu\text{m/s}$. For CAFM imaging, obtained simultaneously with topography imaging (Fig. 3), we applied a -2.5 V DC bias to the sample and a highly sensitive CAFM module (Veeco) was used to sense the current passing through a

conducting Pt/Ir coated n-type Si tip (SCM-PIC, Veeco) with spring constant of 0.2 N m^{-1} .

The conducting tip scanned over the sample in contact mode at a speed of $12 \text{ } \mu\text{m s}^{-1}$, with a normal loading force of 40 nN. For KPFM (data reported in Fig. 4c), we used a conducting Pt/Ir coated n-type Si tip (Veeco) with spring constant of 3.0 N m^{-1} , resonance frequency of 78 kHz, and a quality factor of ~ 150 . A two-scan lift mode was used to collect the contact potential data. In the first scan, the tip was operated in tapping mode at the cantilever resonant frequency with a mechanical piezo-oscillator to collect the topographical signal. In the second scan, the tip was lifted 20 nm above the sample, and a 6 V peak-to-peak AC voltage was applied to the tip at the cantilever resonant frequency. A lock-in amplifier and a servo feedback unit was used to track the cantilever oscillation at the resonant frequency and record the contact potential (ϕ).

We repeated the room temperature friction, conductive and Kelvin probe force microscopy experiments several times after hours and days following the thermally induced reduction. In this way, any desorbed water during the thermal processing could re-adsorb on the surface. Of course, if the material changes from GO to graphene, less water would re-adsorb, but then this is just another confirmation of a successful reduction.

3. TCNL tip-surface contact local temperature calibration

The temperature at the tip-surface interface can be estimated by following a method described in the literature (7-8). The thermal resistance of the tip-surface contact (R_{ts}) is the sum of three thermal resistances, namely the tip thermal resistance (R_t), the interface resistance (R_{int}), and the sample spreading resistance (R_{spread}):

$$R_{ts} = R_t + R_{int} + R_{spread} .$$

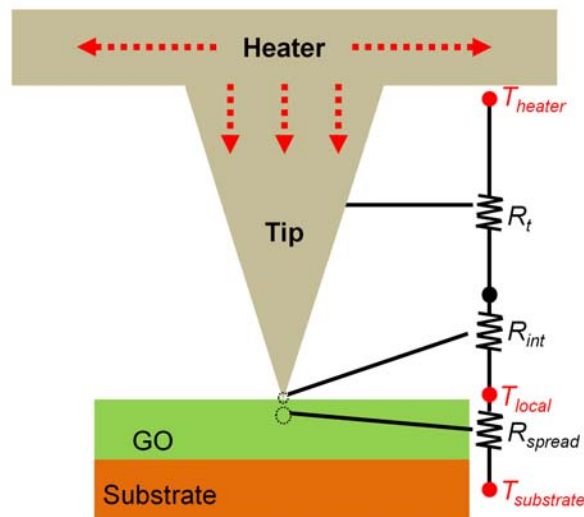


Figure S1. Schematic of TCNL Tip-Surface Point Contact

According to the calculation of Dürig et. al. the heating efficiency (C), defined as the ratio between the rise in tip-surface local temperature, T_{local} ($^{\circ}\text{C}$), and the rise in cantilever heater temperature, T_{heater} ($^{\circ}\text{C}$), can be expressed as:

$$C = \frac{T_{local} - RT}{T_{heater} - RT} = \frac{R_{spread}}{R_{tip} + R_{int} + R_{spread}},$$

where RT stands for room temperature (δ).

In the tip, the thermal resistivity increases with respect to the bulk silicon because of enhanced phonon scattering with boundary surfaces. The thermal resistance of the tip, R_{tip} , can be estimated using predictions for the thermal conductivity of silicon nanowires, which is of the order of 10^7 K W^{-1} .

The thermal resistance of the interface, R_{int} , usually depends on the interface quality and the contact pressure. In the simplest case, we assume a single asperity with a contact radius a and a constant r_{int} , which depends on the materials involved and the pressure:

$$R_{int} = \frac{r_{int}}{\pi a^2}.$$

The interface can be treated as a scattering site for phonons in silicon. Experimentally, r_{int} is in the order of $10^{-8} \text{ K m}^2 \text{ W}^{-1}$. Therefore, we expect $R_{int} \sim 1.3 \times 10^8 \text{ K W}^{-1}$ for $a \sim 5 \text{ nm}$.

The spreading resistance can be calculated as:

$$R_{spread} = \frac{1}{\pi a k_{GO}} \int_0^{\infty} \left(\frac{1+K}{1-K} \right) J_1(x) \sin(x) \frac{dx}{x^2},$$

where the thermal conductivity parameter K is defined as:

$$K = \left(\frac{1 - \frac{k_{sub}}{k_{GO}}}{1 + \frac{k_{sub}}{k_{GO}}} \right),$$

and $J_1(x)$ is the first order Bessel function, k_{GO} and k_{sub} are the thermal conductivities of the graphene oxide and substrates (SiO_x or SiC), respectively (9).

For the thermal tip in contact with GO_{epi} , assuming a 5 nm contact radius, 16 nm GO thickness, SiC substrate thermal conductivity $k_{sub} \sim 370 \text{ W m}^{-1} \text{ K}^{-1}$ (10), and GO thermal conductivity $k_{GO} \sim 1.9 \text{ W m}^{-1} \text{ K}^{-1}$ (11-12), we can estimate a spread thermal resistance $R_{\text{spread}} \sim 2.3 \times 10^7 \text{ K W}^{-1}$, and the heating efficiency $C_{\text{epi}} = 0.14$ (for Fig. 3 and Fig. 4).

For the thermal tip in contact with a GO flake, with a 5 nm contact radius, 1 nm GO thickness, SiO_x substrate thermal conductivity $k_{sub} \sim 1 \text{ W m}^{-1} \text{ K}^{-1}$ (13), and GO thermal conductivity $k_{GO} \sim 1.9 \text{ W m}^{-1} \text{ K}^{-1}$ (11-12), we can estimate a spread thermal resistance $R_{\text{spread}} \sim 4.0 \times 10^7 \text{ K W}^{-1}$. Because there is an imperfect thermal contact between the GO flake and the SiO_x substrate, there will be scattering at the interface. This thermal contact resistance between the GO flake and the substrate is at least as big as R_{int} . Therefore, the heating efficiency for GO flake system $C_{\text{flake}} = 0.55$ (for Fig. 1 and Fig. 2).

The temperature of the heater is rigorously measured and extremely well understood. It can be calibrated with accuracy up to 600 °C by means of Raman spectroscopy, and resistance vs. voltage measurements across the resistively heated cantilevers as explained in reference (5). However, for higher temperatures nonlinear effect could be present.

Temperature calibration is less well understood and has not been directly measured.

In addition, because GO and graphene are layered the above arguments underestimate the tip contact temperature, most likely by a significant amount. Unfortunately, the important scientific debate over the nature of heat flow across atomically layered materials remains unresolved. It has been established, though, that the thermal conductivity across layered solid films can be smaller than the amorphous limit (14). We consider heat flow from the cantilever heater region through the tip, to graphene, graphene oxide and SiC. This thermal conduction path can be approximated as one-dimensional, since the main thermal resistances are in series between the heater and the heat sink. It is reasonable to assume that the main thermal resistances in the system are the interfacial thermal resistances between the tip and the graphene, and between the graphene oxide and the SiC substrate. We consider these thermal resistances to be approximately equal, because the tip-substrate contact diameter is on the order of the thickness of the graphene/graphene oxide

film. One-dimensional heat flow through the thickness of the graphene/graphene oxide film yields a linear temperature profile in the film. Thus for a tip-substrate interface temperature of 800 °C, the top 87.5% of the graphene/graphene oxide film can be heated to above the reduction temperature threshold of 100 °C. We remark that if the SiC/GO interface has a very high thermal resistance, even more than 87.5% of GO can be reduced in depth.

4. Raman spectroscopy

We compare the Raman spectra obtained from a 20 μm square locally reduced by TCNL at $T_{heater} \sim 1200$ °C to the spectra obtained from extended films of GO_{epi} . Raman spectra were recorded in the backscattering geometry using a Horiba Jobin-Yvon LabRam HR coupled with an Olympus BX41 optical microscope. A 100 \times (0.9 NA) objective focuses the laser beam of wavelength 532 nm on the sample to a power density of about 1 mW μm^{-2} and a spot size of about 2 μm , small enough to probe one single TCNL rGO_{epi} nanopattern at a time.

The spectra in Fig. S2 show a few cm^{-1} shift of the G peak towards lower frequency when GO_{epi} is reduced, in agreement with previous experiments (15).

The area ratio of the D and G bands is a measure of the size of sp^2 ring clusters in a network of sp^3 and sp^2 bonded carbon (15). The I(D)/I(G) ratios (which are obtained from the same patterns used in the 4 probe measurements) are slightly increasing with increasing temperature, in agreement with previous reports (16-17). Above the power of 21 mW, however, the I(D)/I(G) ratio is observed to decrease again. This behavior can be due to the following reasons. The temperature at the tip-sample interface may become lower due to losses associated with heat radiation from the cantilever at high temperatures, i.e., the heating efficiency of the probe decreases. Another possibility could be that, according to Mattevi *et al.* (15), if the sample is heated to very high temperatures (around 1000 °C), the I(D)/I(G) ratio eventually decreases since the lattice structure becomes more ordered with high temperature annealing. This analysis indicates that the sp^2 cluster size in GO_{epi} and TCNL rGO_{epi} is about 5 nm, similarly to previous reports.

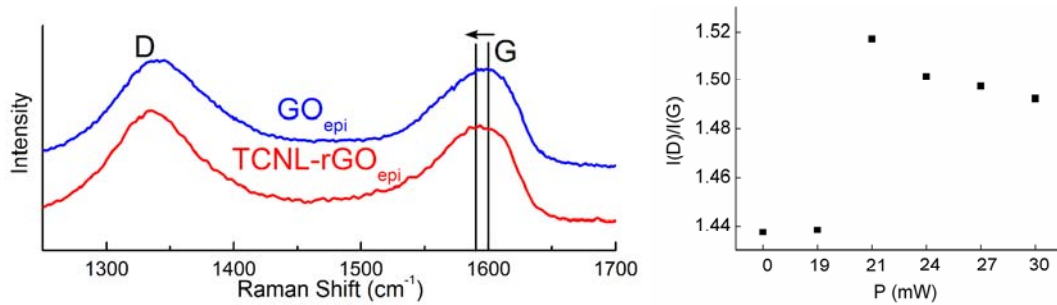


Figure S2. (Left) Raman D band and G band spectra of GO_{epi} , and reduced GO_{epi} by TCNL at $T_{\text{heater}} \sim 1200$ °C. (Right) Intensity ratios of the areas underneath the D band and G band as a function of the cantilever power (P).

5. Microscopic four-probe electrical transport measurements

Electrical transport measurements (Fig. 4 in the main manuscript) were performed in an UHV Omicron Nanoprobe system (2×10^{-10} mbar) with four independently controlled STM tips and a high resolution SEM which allows nanoscale positioning of the tips. Electrochemically etched tungsten probes (tip diameter < 50 nm(18)) were used for the electrical transport measurements. All current–voltage curves were measured using a Keithley 236 source-measure unit programmed with home built data acquisition software. The sheet resistance of a sample can be obtained from $I(V)$ measurements in a square four-point arrangement. As shown in Fig. S3, a linear current $I_{1,2}$ was passed between adjacent tips (T1 and T2) and the potential drop $V_{3,4}$ across the opposing tips (T3 and T4) was recorded as a function of $I_{1,2}$. The sheet resistance from the measurements of

macroscopic sample surfaces (epitaxially grown graphite: EG; oxidized epitaxially grown graphite: GO_{epi} ; and reduced GO_{epi} : rGO_{epi}) was derived from a 2D infinite sheet model, while the sheet resistance of the microscopic $20 \mu\text{m} \times 20 \mu\text{m}$ TCNL reduced GO_{epi} patterns (TCNL- rGO_{epi}) was derived using a Van der Pauw model. The details of the models are given below.

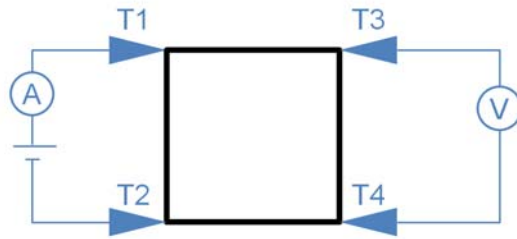


Figure S3. Schematic of microscopic 4-probe electrical transport measurement.

5.1 Two dimensional infinite sheet model

For measurements on macroscopic samples, the probes were placed in a square configuration with $100 \mu\text{m}$ separation between adjoining tips. Since the probes are far away from the edges of the sample which is mm in size, the sample can be regarded as infinitely large and the sheet resistance can be calculated analytically by solving the Poisson equation (19). The sheet resistance of an infinite 2D sheet measured with square four-point arrangement is independent of the probe spacing and can be derived from the

measurements using the equation:

$$R_{sheet} = \frac{\pi}{\ln \sqrt{2}} \frac{\Delta V_{3,4}}{I_{1,2}}.$$

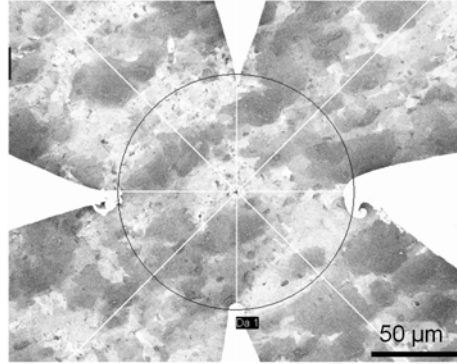


Figure S4. SEM micrograph of 4-point transport measurement of a GO_{epi} film.

5.2 Van der Pauw model

In order to obtain the sheet resistance of a microscopic 20 μm × 20 μm TCNL reduced GO_{epi} pattern (TCNL-rGO_{epi}), the STM tips were placed on the corners of the pattern. Since the surrounding GO_{epi} is highly insulating, the electrical current generated from the source tips (T1 and T2) is confined within the pattern boundary. Therefore, we use the van der Pauw method to calculate the sheet resistance of the TCNL-rGO_{epi} using the equation (20):

$$R_{sheet} = \frac{\pi}{\ln 2} \frac{\Delta V_{3,4}}{I_{1,2}}.$$

The square pattern of TCNL-rGO_{epi} enclosed by solid lines in Figure S5 was obtained by rastering a hot tip on the GO surface, while scanning the entire square only once (left to right is the fast scan direction, and top to bottom is the slow scan direction). Since we scanned 512 lines over an area of 20 μm , the spacing between adjacent scan lines along the slow scan direction is ~ 40 nm. These sheet resistance results indicate the good control and reproducibility of TCNL in every scan-line to produce large micron size patterns.

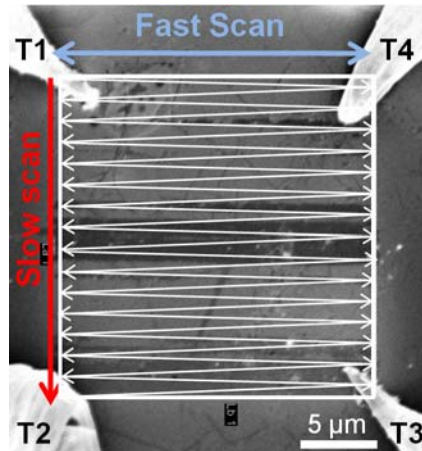


Figure S5. SEM image of the micro 4-probe experiment with a sketch of the tip scan lines during the TCNL reducing. The four conductive probes are shown as T1-T4.

6. Additional height images of reduced GO

The heated tip was scanned over a diamond-shaped area leading to loss of oxygen-rich functional groups and consequently a decrease in height. The height loss is typically 2-5 Å as shown by the cross-section in Fig. S6C.

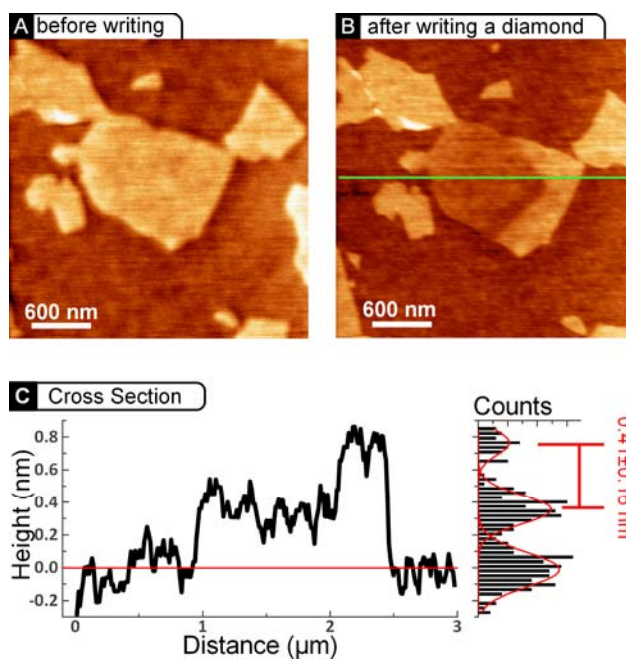


Figure S6. AFM height images of a GO flake before (A) and after (B) reduction. The height profile of (B) is shown in (C).

7. Additional CAFM data

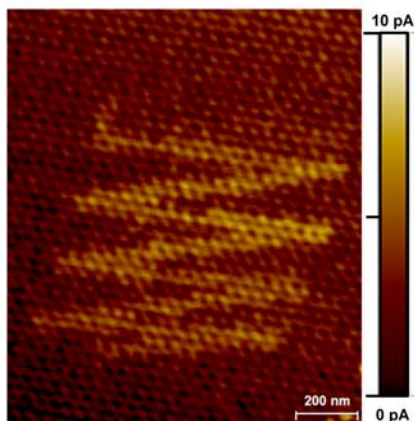


Figure. S7. CAFM current image obtained by applying a 2 V DC bias between a platinum tip and the sample substrate, at a normal load of 8 nN and with a linear scanning speed of $12 \mu\text{m s}^{-1}$. The zigzag nano-pattern of rGO was produced by TCNL on a **2-layer** GO film epitaxially grown on a SiC substrate. The peak current values are around 10 pA, consistent with the current values reported in Fig. 3 where the current was measured by applying a larger normal load and bias.

8. Additional data of KPFM and transport measurements

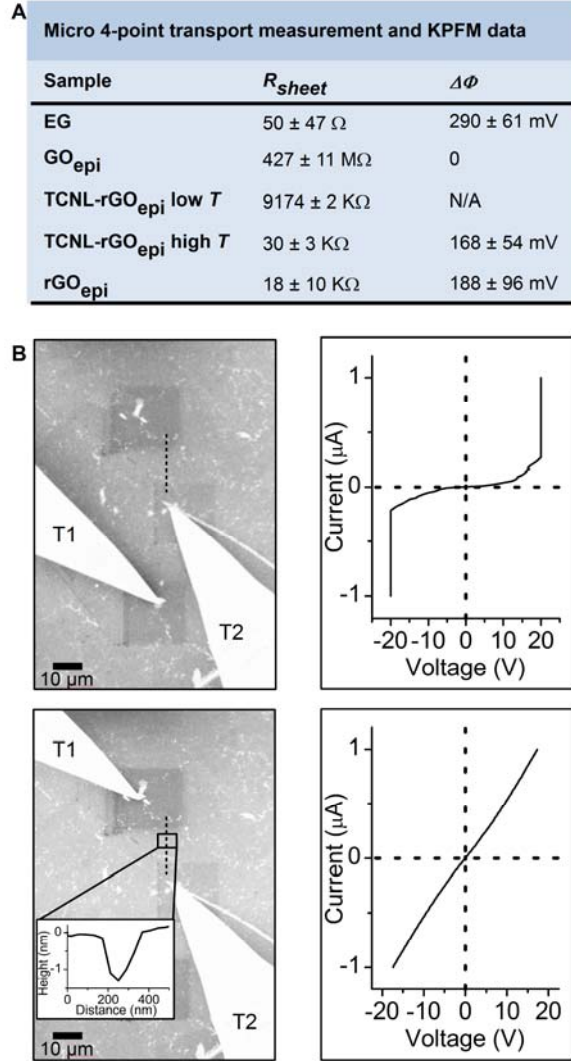


Figure. S8. Additional data of KPFM and transport measurements. (A) This table presents the values of sheet resistance, R_{sheet} , measured by 4-point transport measurements, and the contact potential change ($\Delta\Phi$) between GO_{epi} and each listed sample (EG, rGO_{epi}, and TCNL-rGO_{epi}, respectively). (B) (Left) SEM micrographs of the configuration used for two-point transport measurements when the tips are positioned between 2 rGO_{epi} squares without (top), and with (bottom) TCNL-rGO_{epi} nanoribbon in between. The AFM cross section of the nanoribbon is shown as inset of the bottom SEM image. (Right) I-V curves obtained by two point measurement of current passing between two rGO_{epi} squares with no nanoribbon in between (top curve), and between two rGO_{epi} squares with a nanoribbon in between (bottom curve).

References and Notes:

1. X. S. Wu *et al.*, *Phys. Rev. Lett.* **101**, 026801 (2008).
2. C. Berger *et al.*, *Science* **312**, 1191 (2006).
3. J. Hass *et al.*, *Phys. Rev. Lett.* **100**, 125504 (2008).
4. W. S. Hummers, R. E. Offeman, *J. Am. Chem. Soc.* **80**, 1339 (1958).
5. J. Lee *et al.*, *J. Microelectromech. Syst.* **15**, 1644 (2006).
6. V. Palermo, M. Palma, P. Samori, *Adv. Mater.* **18**, 145 (2006).
7. B. A. Nelson, W. P. King, *Nanosc. Microsc. Therm.* **12**, 98 (2008).
8. B. Bhushan, H. Fuchs, *Applied Scanning Probe Methods IV: Industrial Applications*. (Springer, Berlin, 2006).
9. M. M. Yovanovich, J. R. Culham, P. Teertstra, *IEEE T. Compon. Pack. A* **21**, 168 (1998).
10. M. E. Levinshstein, S. L. Rumyantsev, M. S. Shur, Eds., in *Properties of Advanced Semiconductor Materials GaN, AlN, SiC, BN, SiC, SiGe*. (John Wiley & Sons, New York, 2001).
11. A. J. Bullen, K. E. O'Hara, D. G. Cahill, O. Monteiro, A. von Keudell, *J. Appl. Phys.* **88**, 6317 (2000).
12. E. Cappelli, C. Scilletta, S. Orlando, V. Valentini, M. Servidori, *Appl. Surf. Sci.* **255**, 5620 (2009).
13. R. Kato, I. Hatta, *Int. J. Thermophys.* **26**, 179 (2005).
14. C. Chiritescu *et al.*, *Science* **315**, 351 (2007).
15. C. Mattevi *et al.*, *Adv. Funct. Mater.* **19**, 2577 (2009).
16. S. Stankovich *et al.*, *Carbon* **45**, 1558 (2007).

17. H. Kang, A. Kulkarni, S. Stankovich, R. S. Ruoff, S. Baik, *Carbon* **47**, 1520 (2009).
18. J. E. McKendry *et al.*, *Nanotechnology* **19**, 085201 (2008).
19. T. Kanagawa *et al.*, *Phys Rev Lett* **91**, 036805 (2003).
20. L. J. van der Pauw, *Philips Res. Repts.* **13**, 1 (1958).